Multi-objective distributed control of WT-PV-BESS integrated weak grid via finite time containment

Linyun Xiong [a,*], Yinfang Zhu [a], Sunhua Huang [b,*], Shiwei Guo [a], Changyu Ban [a], Penghan Li [c], Muhammad Waseem Khan [d], Tao Niu [a]

[a] School of Electrical Engineering, Chongqing University, Chongqing, 400044, China
[b] Department of Electrical Engineering, The Hong Kong Polytechnic University, Hong Kong 999077, SAR, China
[c] Northwest Branch of State Grid Corporation of China, Xi'an, 710049, China
[d] Interdisciplinary Research Center for Renewable Energy and Power Systems (IRC-REPS), King Fahd University of Petroleum & Minerals, Dhahran, 31261, Saudi Arabia

ARTICLE INFO

ABSTRACT

This paper proposes a finite time containment control scheme to achieve distributed control of a weak grid which is integrated with photovoltaic (PV), wind turbine (WT) and battery energy storage system (BESS). Taking advantage of the containment control in multi-dimensional control, we proposed a multi-objective control scheme of the WT-PV-BESS system in a weak grid, wherein four control objectives are specified, namely, bus voltage regulation, grid frequency control, peak load shaving and economic benefits optimization for the system operator. Firstly, the sizing approach of BESSs to fulfill the operation mission requirements is proposed; meanwhile, the general coordination strategy for the PV, WT and BESS to achieve the demand–supply balance is proposed. Subsequently, the predefined four control objectives are modeled and transferred into the long/short time frame operational constraints of the BESSs. Afterwards, the finite time containment control algorithm is proposed to force the BESSs into achieving containment status within prescribed time. Simulation case studies are conducted on a modified IEEE 9-bus system to show the effectiveness and performance of the proposed scheme.

1. Introduction

WITH the gradual replacement of traditional fossil energy with renewable energy including wind and solar energy, power system is experiencing a major technological revolution. According to the report of the International Energy Agency, the installed capacity of renewable energy worldwide is about to reach 1150GW by 2022 with the accelerated deployment of investments and facilities in cultivating green energy sources [1]. Therefore, the future power grid is expected to be greener, more self-supplementary and utilizing distribution generation (DG) instead of massive centralized generation.

For all the modern power grid configuration, remote areas are becoming more dependent on the renewable energy sources (RESs) due to the vast availability of energy sources like solar, wind, biomass and hydro. In the meantime, the advancements in power electronic technologies as well as electrical machine designs effectively decreased the cost and enhanced the power quality of RESs, leading to higher autonomy of the remote and weak grids [2]. Nevertheless, the stochastic nature of RESs and the phase-out of the synchronous generators (SGs) have brought about critical challenges to the system stability and operation, especially the significant loss of system inertia which leads to severer frequency instability issues that may trigger multiple frequency dependent emergency incidents [3–5]. Moreover, the remote area weak grid may lack the sufficient short-circuit level, which reduces its system strength and makes it prone to high voltage sensitivity [6]. Under some extreme operation conditions, the stable operation of the weak grids cannot be ensured and the power output of RESs may be curtailed or even disconnected, leading to generation deficit and potential frequency control issues [7,8]. Meanwhile, the stochastic nature of wind and solar power will cause further mismatches between the generation and the load, causing voltage sages during peak load condition and voltage surges during peak generation condition when there is reverse power through the distribution lines [9]. Therefore, within a remote area weak grid, voltage and frequency stability are two of the pivot missions for the control and configuration design of the network.

Apart from the aforementioned aspects, there are other issues that

need to be resolved in remote area weak grids, i.e., power quality problem and the efficiency of energy harvesting or utilization. For the RESs, the stochasticity of wind speed or solar radiation will inevitably result in fluctuation of the supplied power, even with the improvement approaches like power electronic modulation [10]. Such issue will become more prominent and intolerable when the share of RESs is large enough in the grid. Moreover, in energy harvesting, the current mainstream approaches like the maximum power point tracking (MPPT) are capable of capturing the maximum available energy from the natural environment [11,12]. Nevertheless, in the traditional demand–supply mode, the generation will also be decided by the demand, which may future lead to the waste of natural energy with power generation curtailment schemes, as the excessive power cannot be stored in the grid for future usage reserve.

With the rapid development of electrochemistry and material science, ESSs, especially battery based ESSs (BESSs) have rising growing interest in power and energy societies. Due to its high flexibility, fast response and high reliability, BESSs are believed to be a kind of feasible solution to enable the smooth integration and consumption of RESs in the future and are attached with strategic importance in various grid expansion and planning projects [13]. For small scale grids, BESSs are being utilized to resolve several technological bottlenecks as mentioned above. For isolated grid frequency regulation, several BESS based control schemes and system configurations are being developed. For example, in [14], the authors proposed a droop-type lead-lag controlled BESS for mitigating the impact of PV generation on the grid's primary frequency control, along with an adaptive state-of-charge (SoC) recovery strategy; in [15], the authors proposed an adjustable SoC limit based control approach for BESSs to assist the load frequency control (LFC) of an isolated power system, wherein the optimal sizing and operation scheme of the BESSs is also developed to achieve highest profitability of the devices; in [16], a fast frequency regulation scheme based on model predictive control with the assistance of BESS is proposed. Apart from that, BESSs are also utilized to enhance the voltage stability of a weak grid. In [17,18], the authors proposed to utilize BESSs to absorb the excessive power during peak PV generation period to mitigate the voltage rise issue caused by reverse power flow, wherein a distributed control scheme is adopted for BESSs SoC regulation; in [19], a coordinated control approach for the grid-connected PV and BESSs is proposed to address the voltage rise and dip problems in a rural and urban distribution network, wherein the reactive capacity of the PV combined with the droop-based BESS system is cultivated for voltage profile improvement.

Despite the fact that various control and energy management approaches are proposed to assist BESSs and DGs in grid service, one of the major drawbacks of the existing literatures lie in that they can only address a single control objective, i.e., frequency control [14–16], voltage regulation [17–19], optimal energy harvesting [20,21], demand response [22], or peak shaving [23]. Under most circumstances, the aforementioned objectives should be fulfilled simultaneously in order to maintain optimal operation and system stability of the grid, which requires the complicated and comprehensive design of a control and energy management system integrating the existing approaches. Thus, to simplify the control method and control system configuration design, this paper aims to propose a multi-objective control methodology for a WT-PV-BESS integrated weak grid via a kind of novel distributed control method, namely, the finite time containment control (FTCC). Originated from the conventional leader–follower distributed control framework, the containment control employs two or more leaders to direct the followers' agents toward the respective targets in different dimensions [24]. Thus, containment control is capable of constraining all the agents' status within a convex hull determined by the system operation constraints, achieving multi-dimensional consensus among the leaders and followers. With this feature, it will be possible for the containment control to achieve multi-objective distributed control of WT-PV-BESS systems in weak grids with different mission requirements. In the

control framework design, four grid operation control missions will be targeted, i.e., frequency control, voltage regulation, economic benefits maximization, and peak shaving. The four missions will be transformed into four control set points of the BESS's SoC and form a four-dimensional convex hull, and four leading BESSs will be selected as the leader to guide the behavior of the followers and constrain the follower BESSs to operate within the convex hull in a consensus manner. In this manner, the BESSs will behave in a cooperative way to assist the WT and PV to achieve the four control objectives. Therefore, the main contribution of this paper is organized as follows:

- The overall framework of a WT-PV-BESS is developed in a weak grid to suit the mission requirements of frequency control, voltage regulation, peak shaving and economic benefits maximization, where the optimal sizes of the BESSs are determined;
- A multi-objective control framework for Wind-PV-BESS is proposed to transform the prescribed control objectives into the set points of the BESSs' SoC and form a convex hull;
- A FTCC approach is developed for distributed control of the BESSs to achieve the co-achievement of the prescribed four objectives with a single control design, which is capable of reaching the convergence status within finite time regardless of the state variable initial state.

The remainder of this paper will be organized as follows: Section II will introduce the overall system framework of the proposed WT-PV-BESS and discuss the formulation of the multi-objective control scheme for the target system; Section III proposes the FTCC approach; Section IV conducts the simulation case studies; Section V gives a brief conclusion of this paper.

2. Problem formulation for control objectives

A. System Configuration

In this paper, the system configuration of the weak grid with integration of Wind-PV-BESS system is shown in Fig. 1. In Fig. 1, the doubly-fed induction generation (DFIG) WT, PV array and the BESSs are operating in a cooperative manner to achieve the prescribed four control missions. For the WT, a frequency droop control is designed couple its rotor speed with the grid frequency to ensure that it is frequency responsive. In Fig. 1, the MPPT curve of the WT is approximated by a

Fig. 1. Proposed Frequency Support Basic Framework.

polynomial $\omega_{ref} = aP_s^2 + bP_s + c$ in order to simplify the analysis, where ω_{ref} refers to the reference rotor speed, Ps denotes the actual power output of the WT, a , b ,c are the coefficients of the polynomial. In the control of WT rotor speed, we utilize a two-stage variable coefficient based control scheme, where the adaptive control gain $k = 1 + \Delta\omega_r/\omega_r^0$ is designed to adaptively control the rotor speed, where $\Delta\omega_r$ is the rotor speed deviation and it is associated with the system frequency deviation, and ω_r^0 is the initial rotor speed [25].

The PV arrays, on the other hand, will be operating in the MPPT status to ensure that the maximum solar energy has been captured, regardless of the local load condition. It is connected to the grid via a boost converter and the local BESSs via a bidirectional converter. Therefore, it is either supplying the local load or charging the distributed BESSs depending on the instantaneous power demand–supply balance. The BESSs, on the other hand, will be serving as the coordinator to achieve the power balance when the power supply from the DGs cannot reach their prescribed quota in the initial network planning, or that there is excessive power output from the DGs. Therefore, in the control framework design of this paper, the four control objectives will be transformed into the operation constraints of the distributed BESSs.

B. Coordinating Strategy for WT, PV and BESS

Due to the high operation flexibility and fast response merits of BESS, it has the potential of enhancing the grid integration performance of WT and PV, especially in power supply quality enhancement, frequency control and voltage regulation. The designed coordination strategy for the WT, PV and BESSs is shown in Fig. 2. In Fig. 2, the power outputs of the SGs, WTs and PVs are stacked to better illustrate the supply–demand balance. The load profile is assumed to be the typical residential type. In the researched weak grid, it is assumed that the total installed power capacities of the synchronous generators (SGs), WT and PV account for 50 %, 30 % and 20 % of the nominal load level, respectively. Therefore, in an ordinary day in the summer season, as the power output of SGs can be more controllable and predictable, the SGs will maintain relatively stable contribution to support the load. The WTs and PVs will serve to bridge the remaining demand gaps in a day. Different from the WTs, the PV arrays will only generate power in the specific time ranges (7:30–18:30 during summer season) in a sunny day.

To achieve maximum capturing and consumption of the green energy, it is required that the WTs and the PVs remain MPPT status across the entire operation day unless additional control missions are applied. Nevertheless, the stochasticity and unpredictability of wind and solar energy will significantly impact the availability of power supply. Therefore, the BESSs will be utilized to achieve the balance between the demand and the supply side: when there is power output surplus during the load's valley period, say, 23:00–6:00, the BESSs will be in the charging status to absorb the extra power and avoid curtailment of wind power, as shown in the green area of Fig. 2; when the overall load level exceeds the overall power output during the peak times, say, 10:00–12:00 and 17:00–20:30, the BESSs will be in the discharging
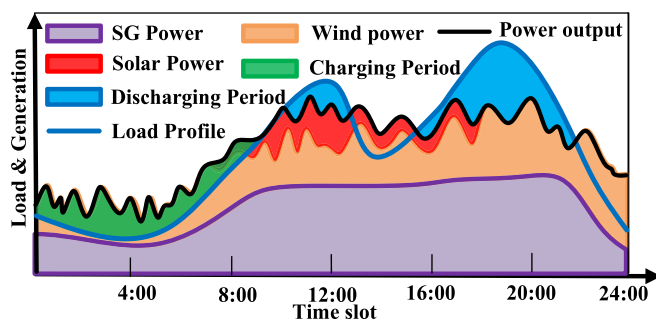
status to support the load, as shown in the blue area in Fig. 2. Therefore, in this paper, the primary coordination strategy between the PV, WT and BESSs is given as

$$P_{BESS}(t) = P_l(t) - P_{SG}(t) - P_{WT}^{MPPT}(t) - P_{PV}^{MPPT}(t) \tag{1}$$

where $Pl(t)$, $PSG(t)$, $P_{WT}^{MPPT}(t)$ and $P_{PV}^{MPPT}(t)$ represent the instantaneous load, SG power output, WT power output and PV power output, respectively; PBESS(t) is the power output/input of BESS. In Eq. (1), positive value indicates power output (discharging), while negative value indicates power input (charging).

C. Sizing of BESS Power and Energy Capacity

It can be seen in the coordination strategy that BESSs need to be deployed to serve as backup system for load support and mitigate the impact of randomness from the wind and solar energy. Therefore, the power capacities of the BESSs need to be specified in accordance with the peak shaving and load support mission. Consider the maximum load level in a day as P_l^M, the lowest total power output of the WT and PV are P_{WT}^m and P_{PV}^m, respectively, then the needed power capacity for the BESSs is

$$\sum_{i\in\mathscr{I}} P_{BESS,i} = (1 - \lambda_{SG})P_l^M - P_{WT}^m - P_{PV}^m \tag{2}$$

where λ_{SG} denotes the share of SGs in load supply.

For the ESS's energy capacity, we have

$$\sum_{i\in\mathscr{I}} E_{BESS,i} = \int_{t_1}^{t_2} P_{BESS}(t)dt \tag{3}$$

where t1 and t2 denote the beginning and end time slots of the peak load duration in a day, respectively.

D. Transforming Control Objectives into BESS's Operation Constraints

1) Frequency regulation with WT and BESS

Firstly, consider the coordination of WT and BESS in grid frequency regulation, the WT will experience two stages to smoothly regulate the grid frequency, namely, the rotor speed decreasing stage and the rotor speed restoration stage. In the first stage, the rotor speed of WT will be decreased to inject extra power to the grid for frequency regulation, and we have

$$P_{desire} = -J\omega_r \frac{d\omega_r}{dt} \tag{4}$$

where J is the inertia moment of the WT, P_{desire} is the desired power from the WT which is prescribed by referring to the assignment of the WT and BESS. Based on (4), we have

$$\int_0^t \omega_r d\omega_r = -\frac{P_{desire}}{J}\int_0^t dt = -\frac{P_{desire}}{J}t \tag{5}$$

which gives

$$\omega_r(t) = \sqrt{\omega_r^2(0) - 2 \times \frac{P_{desire}}{J} \times t} \tag{6}$$

where t is the time needed for the frequency to be restored to the allowable range, $\omega_r(0)$ is the initial rotor speed. In the control design, the desired power for each WT and the time t will be specified based on the system's frequency dynamics, and the rotor speed $\omega_r(t)$ will be controlled via a PI controller which transfers the reference rotor speed to the reference torque applied to the rotor.

In the second stage where the system frequency is recovered to the allowable range, the rotor speed has to be recovered to the MPPT status as it is drifted away from the optimal operation point. During this stage,

Fig. 2. Proposed Coordination Strategy for WT, PV and BESS.

the WT will absorb energy to increase its rotor speed until it reaches the MPPT reference value, which may cause secondary frequency dip caused by power output reduction from the WT. Therefore, to mitigate such effect on the system frequency, a rotor speed buffer function is designed to smoothly recover the rotor speed, and the schematic of the rotor speed recovery control is given in Fig. 3 [26]. Therefore, the reference rotor speed is given as

$$\omega_{ref} = (\omega_{MPPT} - \omega_r)f(\Delta\omega) + \omega_r \tag{7}$$

where ω_{MPPT} denotes the rotor speed under the MPPT status.

In the meantime, the BESS will assist the WT in frequency support and ensure the system's frequency stability. BESSs will serve two purposes: 1) to provide supplementary power in case that the converted kinetic energy from the WT is not sufficient to render the sudden load increases; 2) to assist the rotor speed recovery of WT to prevent secondary frequency drop. In the frequency support stage, the BESS will act with the frequency droop characteristic as shown in Fig. 4 [14]. In Fig. 4, a non critical frequency band (NCFB) which has the half-width of 0.004p.u of the nominal value is designed, where BESS will remain its current status. When the grid frequency $f_{grid} > f_{ch}$, the BESS will consume the surplus power by shifting to the charging mode, and delivers power when the grid frequency $f_{grid} < f_{disch}$. When the BESS is activated due to frequency deviation, the power output reference dPref will change linearly with the deviation of frequency with the NCFB. The maximum charge or discharge power (P_{ch-max} or $P_{disch-max}$) will be activated for the maximum frequency deviation (Δf_{max} or Δf_{min}) as long as the SoC of the BESS remains within the upper and lower bounds SoCmax and SoCmin. Thus, the droop characteristics of the BESS can be written as

$$dP_{ref} = \frac{1}{K_{BESS}}\left(f_{ref} - f_{grid}\right) \tag{8}$$

where K_{BESS} denotes the droop parameter of the BESS, f_{ref} is the reference frequency (1 ± 0.004p.u.).

In the rotor speed recovery stage, the BESSs will start to inject power to the grid to support the rotor speed recovery of WT at time slot either when the grid frequency is recovered to the safety range, or that the rotor speed is about to across the lower limit. Meanwhile, to further recover the grid frequency to the nominal value, the BESS needs to yield extra power which is relative to the system frequency deviation. Overall, the stages for the WT-BESS to engage in frequency regulation are shown in Fig. 5. In Fig. 5, four key time slots are labeled with respect to different stages of frequency regulation. At t1 when the grid frequency is lower than the threshold of -0.002 p.u., the WT will convert its kinetic energy into extra power to support the frequency, leading to reduction of its rotor speed; at t2 when the grid frequency continues to drop and is passes the BESS reaction threshold of -0.004 p.u., the BESS will act to output its maximum power to prevent further frequency drop; at t_3 when the grid frequency is recovered to the BESS reaction threshold, the BESS will gradually reduce its power output in order to make sufficient reserve for the rotor speed recovery; at t_4 when the grid frequency is recovered to the WT reaction threshold, the WT will gradually absorb energy to recover its rotor speed, and the BESS have to provide extra
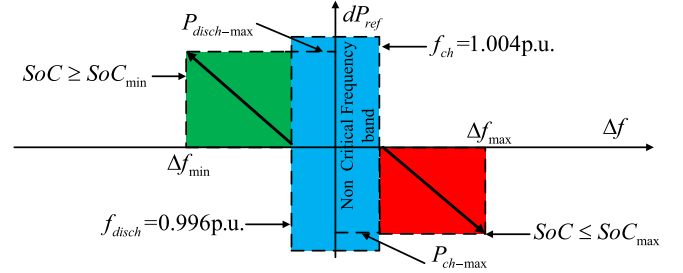
Fig. 4. Frequency droop characteristics of the BESS.
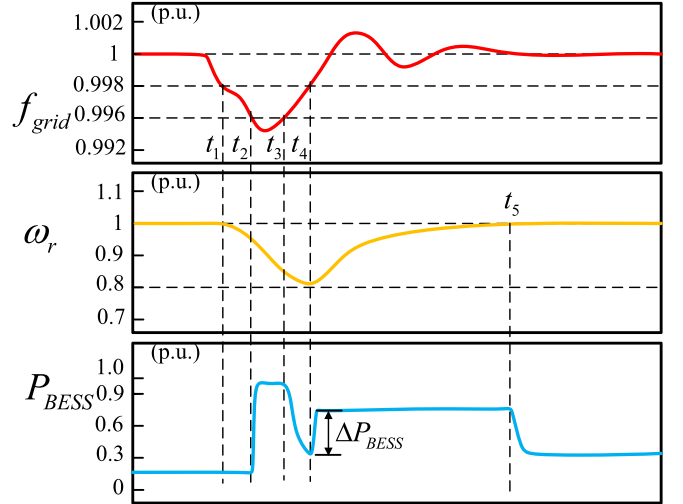
Fig. 5. Frequency regulation stages with WT-BESS.

power to the grid to render the power output reduction from the WT. Based on (5), the extra power provided by BESS in rotor speed recovery at time t_4 is given as

$$\Delta P_{BESS} = \frac{1}{2(t_5 - t_4)}J\left(\omega_r^2(0) - \omega_r^2(t_4)\right) \tag{9}$$

where t_5 is the time slot when the WT has fully recovered its rotor speed.

2) PV Bus Voltage Regulation with BESS.

In a high PV penetrated grid, the overvoltage issue may happen due to the existence of reverse power flow caused by PV generation. When the PV generation cannot be consumed locally, the reverse power flow injected to the PV bus nodes will cause overvoltage issue [17]. Therefore, distributed and local voltage control with BESS is also a key objective in this paper, by which BESS will be utilized to absorb the extra power to prevent overvoltage, and support local loads to prevent under voltage, all of which are accomplished by active power control. The voltage regulation operation range of BESS is shown in Fig. 6. Based on the IEEE standard 1547, the maximum and the minimal allowable
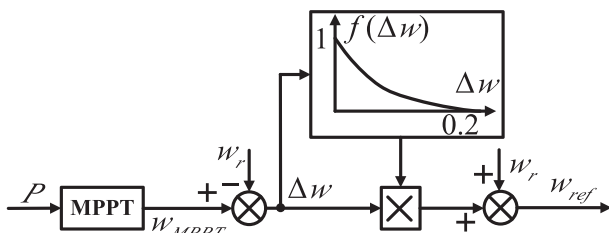
Fig. 3. Utilized rotor speed recover control scheme.
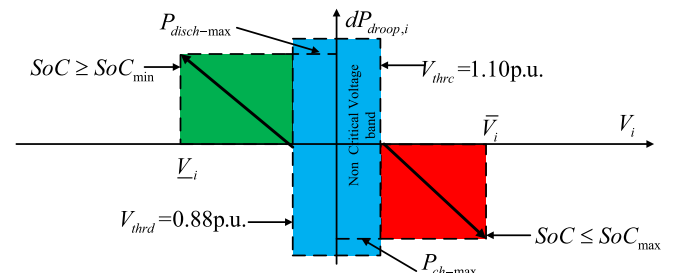
Fig. 6. Voltage regulation for PV bus nodes with BESS.

voltage for a distribution network are 1.1p.u. and 0.88p.u., respectively [27]. Violation of the bus voltage conditions may trigger the disconnection of DGs from the network. Therefore, in Fig. 6, we again specified a non critical voltage band where the BESS will not act to charge or discharge. When the bus voltage is detected to get out of the band, the charging or discharging power of the BESS will be

$$P_{BESS} = \begin{cases} m_d(V - V_{thrd})V < V_{thrd} \\ 0V_{thrd} \leqslant V \leqslant V_{thrc} \\ m_c(V - V_{thrc})V > V_{thrc} \end{cases} \tag{10}$$

where V denotes the bus voltage, V_{thrc} and V_{thrd} are the charging and discharging threshold, respectively; m_c and m_d are the voltage droop coefficients for the charging and discharging mode, as given by [17]

$$m_c = \frac{P_{PV}^{max} - P_L^{max}}{V_{thrc} - V_{nom}} m_d = \frac{P_{PV}^{max} - P_L^{max}}{V_{nom} - V_{thrd}} \tag{11}$$

where P_{PV}^{max} and P_L^{max} are the maximum PV generation and local node in the same bus, respectively; V_{nom} is the nominal voltage at the bus.

3) Peak Load Shaving.

Peak load shaving is another mission for the control design of the WT-PV-BESS system. During the peak load times, the available power supply capacity from WT, PV and DGs may not be capable of fulfilling the demands from the load, leading to frequency drops, voltage dips and load curtailment actions. Therefore, peak load shaving should be accomplished by BESSs. Nevertheless, there are several significant distinctions between peak load shaving and frequency/voltage regulation. Comparing with the former objectives, peak load shaving has a relatively longer time frame as the mission may last for hours; meanwhile, it is subjected to more operational constraints like distribution line power upper bound, transformer power limit, SoC limits, and power losses constraints. Therefore, the former control objectives can be deemed as instantaneous and short term control missions, while the latter one should be treated as a long term objective with more constraints.

In this section, we formulate the problem of peak load shaving as a linear multi-phase branch flow model developed in [28], in which for any branch of the network, we have

$$\Lambda_{ij,t} = s_{j,t}^d - s_{j,t}^g - s_{j,t}^b + \sum_{k \in N_j^+} \Lambda_{jk,t}^{\Phi_j}, t \in T_{peak} \tag{12}$$

$$S_{ij,t} = (aa^H)^{\Phi_{ij}} \text{diag}(\Lambda_{ij,t}), t \in T_{peak} \tag{13}$$

where $s_{j,t}^d$, $s_{j,t}^g$, and $s_{j,t}^b$ denote the complex load, complex DG power injection and complex BESS power injection at time t at bus j, respectively; $S_{ij,t}$ denotes the complex power flow from bus i to bus j at time t; $\Lambda_{ij,t}$ denotes the approximate diagonal entries of $S_{ij,t}$; Φ_j is the phase set of bus j; N_j^+ is the set of the children bus of bus j; $a = [1, e^{-i2\pi/3}, e^{i2\pi/3}]^T$; $v_{i,t}$ denotes the complex voltage at bus i at time t.

In the above model, Eq. (12) represents the network power flow balance during the peak load or generation times. In this process, instead of utilizing the time-of-use electricity prices or other strategies to discourage power usage during peak times, the BESSs are utilized to actively meet the demand, and help to achieve the peak load shaving and valley filling mission by regulating their charging and discharging behaviors: during the peak times, all the BESSs will discharge to meet the demand and fulfil the equation constraint in (12)-(13), and during the valley times, all the BESSs will charge to absorb the energy from the stochastic DGs.

The line current can be approximately captured as

$$\Lambda_{ij,t} = V_n diag(a^{\Phi_{ij}} I_{ij,t}^H), t \in T_{peak} \tag{14}$$

$$l_{ij,t} = I_{ij,t} I_{ij,t}^H, t \in T_{peak} \tag{15}$$

where $I_{ij,t}$ is the complex line current from bus i to bus j at time t; V_n is

the nominal bus voltage; $l_{ij,t}$ denotes the squared current matrix at time t. For the BESS, its power model and operational constraints are given as

$$\text{Re}\left\{s_{i,\varphi,t}^b\right\} = b_{i,\varphi,t}^{dc} - b_{i,\varphi,t}^{ch}, t \in T_{peak} \tag{16}$$

$$0 \leqslant b_{i,\varphi,t}^{ch} \leqslant \mu_{i,\varphi,t} \cdot \overline{S}_{i,\varphi}, t \in T_{peak} \tag{17}$$

$$0 \leqslant b_{i,\varphi,t}^{dc} \leqslant (1 - \mu_{i,\varphi,t}) \cdot \overline{S}_{i,\varphi}, t \in T_{peak} \tag{18}$$

$$\mu_{i,\varphi,t} \in \{0, 1\}, t \in T_{peak} \tag{19}$$

$$SoC_{i,\varphi,t} = SoC_{i,\varphi,t-1} + \left(b_{i,\varphi,t}^{ch}\eta^{ch} - \frac{b_{i,\varphi,t}^{dc}}{\eta^{dc}}\right)\frac{\Delta T}{\overline{E}_{i,\varphi}}, t \in T_{peak} \tag{20}$$

$$SoC^{min} \leqslant SoC_{i,\varphi,t-1} \leqslant SoC^{max}, t \in T_{peak} \tag{21}$$

$$SoC_{i,\varphi,0} = SoC_{i,\varphi,24} \tag{22}$$

$$\left\|\begin{bmatrix} \text{Re}\left\{s_{i,\varphi,t}^b\right\} \\ \text{Im}\left\{s_{i,\varphi,t}^b\right\} \end{bmatrix}\right\|_2 \leqslant \overline{S}_{i,\varphi}, t \in T_{peak} \tag{23}$$

where $b_{i,\varphi}^{dc}$ and $b_{i,\varphi}^{ch}$ denote the charging/discharging power of the BESS at bus i with phase φ; $\mu_{i,\varphi,t}$ is the indicator of the charging or discharging status of BESS at bus i with phase φ at time t; $\overline{S}_{i,\varphi}$ is the power rating of BESS; $SoC_{i,\varphi,t}$ is the state of charge of BESS at bus i with phase φ at time t; η^{ch} and η^{dc} are the charging and discharging efficiency, respectively.

In model (16)-(23), (16)-(19) represent the real power of the BESS; (20) is the SoC updating dynamics of BESS, and (21)-(22) is the operational constraints. (23) is the constraint of the apparent power of the BESS converter to restrict the active and reactive power of the BESS in a coupling way.

4) Economic Benefit.

As electrical power is a kind of commodity in the electricity market, economic benefit is one of the key objectives in the daily operation and control design. In the electricity market, there are diurnal price swings corresponding to the fluctuation of demand in a day. Therefore, when the BESSs are utilized in a day, energy arbitrage approach can be utilized for the system operators and asset owners to improve their economic benefit. Energy arbitrage refers to the behaviors of purchasing power when the prices are low and selling when the prices are high. For the asset owners, energy arbitrary is a key strategy for it to recover its prior stage investment and optimize its overall benefit. For the BESSs, they will be in the charging mode during low price durations and the discharging mode during the high price period. The typical price swings in a day is shown in Fig. 7, where the locational marginal price (LMP) in the day ahead energy market for the Sterling in Massachusetts load node is shown. In energy arbitrage, the potential revenue is a function of the shape of the peak relative to the trough, as well as the round trip efficiency σ_c. Thus, the problem of arbitrage opportunity optimization in a day is given by
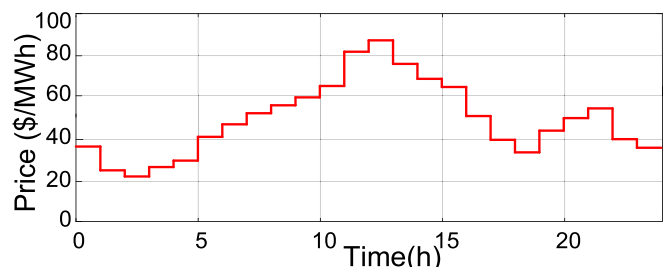

Fig. 7. Typical variations in day-ahead market energy prices.

$$maxTAO = \sum_{i=1}^{24}\left(q_i\sigma_c LMP_{H,i} - q_i' LMP_{L,i}\right) \tag{24}$$

$$s.t. \sum_{i=1}^{24} q_i = \sum_{i=1}^{24} q_i' \tag{25}$$

$$\frac{LMP_H}{LMP_L} \geqslant \frac{1}{\sigma_c} \tag{26}$$

$$(20) - (23) \tag{27}$$

where TAO denotes the total arbitrage opportunity in a day and it is the sum of the hourly arbitrage opportunity; $LMP_{H,i}$ and $LMP_{L,i}$ represent the high locational marginal price and low locational marginal price at the ith time slot, respectively; q_i and q_i' denote the discharge and charge quantity, respectively.

In the above optimization model, (25) aims to ensure that the charged power and discharged power in a day can be balanced; (26) aims to ensure that the arbitrage opportunity is profitable.

3. Robust containment control of BESSs

A. BESSs Modeling.

In the proposed multi-objective control framework, BESSs will play key roles in balancing the power distribution with respect to the time and space dimension of the grid. Thus, the robust containment control algorithm will be applied for the BESSs such that they will be constrained in the convex hull formed by the control objectives. In the control design, N followers and M leaders will be selected. For the leaders, their dynamics [29] are given as follows:

$$\dot{e}_i(t) = -\frac{\rho_i P_{ESS,i}^{max}}{3600 \times C_{ESS,i}} p_i(t) = K_{ESS,i} p_i(t) \tag{28}$$

$$\dot{p}_i(t) = u_i, \quad i \in \mathscr{L} \tag{29}$$

where ρ_i is the charging/discharging coefficient of the ith BESS, $P_{ESS,i}^{max}$ denotes the power rating (MW) of the ith BESS, $C_{ESS,i}$ is the energy capacity (MWh), e_i denotes the SoC of the BESS, $p_i \in [-1,1]$ denotes the power state, $\mathscr{L}$ is the leader set.

For the followers, their dynamics are given by

$$\dot{e}_i(t) = K_{ESS,i} p_i(t) \tag{30}$$

$$\dot{p}_i(t) = u_i + d_i, \quad i \in \mathscr{F} \tag{31}$$

where $\mathscr{F}$ denotes the follower set, the remaining variables are the same as those of Eq. (28)-(29), and d_i is the bounded input disturbance which satisfies $\|d_i\|_\infty \leq \delta$ with $\delta > 0$.

B. Containment Control with Time-Varying Leader SoCs.

Assume the communication graph of the BESSs is denoted by a directed graph $\mathscr{G}$, where each BESS is denoted by a vertex in its vertices set $\mathscr{V}$ and $(i, j) \in \mathscr{E}$ if the jth BESS can receive the information from the ith BESS, where $\mathscr{E}$ is the edge set of the communication graph of BESSs. Let $A_{N+M} \in \mathbb{R}^{(N+M)\times(N+M)}$ and $L_{N+M} \in \mathbb{R}^{(N+M)\times(N+M)}$ denote the adjacency matrix and the Laplacian matrix of the communication graph, respectively. The Laplacian matrix in the following sections is partitioned as

$$L_{N+M} = \begin{bmatrix} L_1 & L_2 \\ 0_{M\times N} & 0_{M\times M} \end{bmatrix} \tag{32}$$

In designing the containment controller, we firstly identify a set of desired sliding surface such that the followers will move along the sliding surface. Subsequently, the distributed control algorithm for the followers will be designed to ensure that they will converge to the

desired sliding surface under the input saturation condition. In what follows, we define $e_F = [e_1, e_2, \cdots e_N]^T$ and $e_L = [e_{N+1}, e_{N+2}, \cdots e_{N+M}]^T$ as the followers' state variable and the leaders' state variable, respectively; define $p_F = [p_1, p_2, \cdots p_N]^T$ and $p_L = [p_{N+1}, p_{N+2}, \cdots p_{N+M}]^T$. Based on the Lemma from [30], the containment control is achieved when $e_F + (L_1^{-1}L_2 \otimes I_N)e_L \to 0$, $t \to \infty$. Hence, here we define $e_d = [e_{d1}, e_{d2}, \cdots e_{dN}]^T = -(L_1^{-1}L_2 \otimes I_N)e_L$, which serves as the desired SoC dynamics of the follower BESSs, and define $p_d = [p_{d1}, p_{d2}, \cdots p_{dN}]^T = -(L_1^{-1}L_2 \otimes I_N)p_L$ as the desired power states of the follower BESSs. In the meantime, we define the containment error as $\widetilde{e}_i = e_i - e_{di}$, and the vector of containment error is $\widetilde{e} = \left[\widetilde{e}_1, \widetilde{e}_2, \cdots \widetilde{e}_N\right]^T$.

Now consider the following sliding mode surface that can decide the ideal trajectory of the BESSs' state variable:

$$s_i = K_{ESS,i} p_i + k_1 \sum_{i=1}^{N+M} a_{ij}(e_i - e_j)$$

$$+ k_2 \tanh\left[\frac{\sum_{i=1}^{N+M} a_{ij}(e_i - e_j)}{\eta}\right] \tag{33}$$

where $k_1, k_1 > 0$ are the sliding surface coefficients, $\eta > 0$ is an infinitely small coefficient. When the state variable reaches the sliding surface, we have

$$e_i = -k_1 \sum_{i=1}^{N+M} a_{ij}(e_i - e_j) - k_2 \tanh\left[\frac{\sum_{i=1}^{N+M} a_{ij}(e_i - e_j)}{\eta}\right] \tag{34}$$

Therefore, for the containment error vector we have

$$\dot{\widetilde{e}} = -k_1(L_1 \otimes I_N)\widetilde{e} - k_2 \tanh\left[\frac{(L_1 \otimes I_N)\widetilde{e}}{\eta}\right] - p_d \tag{35}$$

For the designed sliding surface, we made the following assumptions: For the follower BESSs in the communication graph, at least one of the leader BESS is reachable from the follower BESS.

For the follower BESSs, we propose the following control input

$$\dot{\widetilde{e}} = -k_1 \sum_{i=1}^{N+M} a_{ij}(p_i - p_j) - \frac{k_2}{\eta}\left\{1 - \tanh^2\left[\frac{\sum_{i=1}^{N+M} a_{ij}(e_i - e_j)}{\eta}\right]\right\}$$

$$\times \left[\sum_{i=1}^{N+M} a_{ij}(p_i - p_j)\right] - k_3 sgn(s_i) \tag{36}$$

where $k_3 > \hat{I}$ is a positive constant.

With the above assumption, the designed sliding surface (33), and the controller input (36), we have the following theorem:

Theorem 1. *On the defined sliding surface $s_i = 0$, the global containment control for system (28)-(29) and (30)-(31) is achieved if the following condition holds:*

$$\lim_{t \to \infty} \|e_i(t) - e_{di}(t)\|_2 \leqslant \|L_1^{-1}\|\sqrt{\frac{2k_2 N q_{max}^2 H_{max} \upsilon}{k_1 q_{min} \gamma_{min}(W)}}\sqrt{\eta} \tag{37}$$

where q_{max} and q_{min} are defined in (A1), v is a to be designed parameter related $\widetilde{e}$, η is a positive constant that can be arbitrarily small; $H_{max} = \max\{\sum_{j=N+1}^{N+M} a_{ij}, i = 1, 2, \cdots, N\}$. The proof of theorem 1 is given in the Appendix.

4. Case studies

To evaluate the effectiveness and performance of the proposed FTCC approach and the coordination framework, simulations are conducted on a modified IEEE 9-Bus power system with relatively high renewable

power penetration, as shown in Fig. 8. In this test system, a synchronous generator (SG), a diesel generator and a WF are the main power sources with the capacity of 1.8 MW, 1.7 MW and 1.6 MW, respectively. Five PV stations are integrated at buses 3, 5, 6, 7 and 8 with the capacities of 240 kW, 220 kW, 210 kW, 180 kW and 160 kW, respectively. Meanwhile, seven BESSs are installed at bus 1, 3, 5, 6, 7, 8 and 9, respectively. Based on Eq. (2) and (3), the power and energy capacities for the BESS to meet the multi-objective control requirements are 168 kW/988kWh, 171 kW/1076kWh, 135 kW/1228kWh, 109 kW/898kWh, 156 kW/1032kWh, 152 kW/1308kWh, 124 kW/1147kWh, respectively. The system supplies the maximum total load of 6.5 MW.

4.1. Case 1: Coordination results under different operating conditions

Firstly it is essential to test the performance of the proposed coordination approach under different operation conditions. The expected outcome of the proposed coordination strategy is to achieve the balance between the demand and the supply under different level of renewable energy availability with the autonomous shifting of BESSs. In this simulation case, three typical operation scenarios are assumed to test the performance of the scheme, namely, steady wind speed condition during peak load time (near 12:00am), variable wind speed condition during peak load time, and variable wind speed condition during valley load time (near 23:00). During the peak load time, the load is set at 5 MW from 12:00–12:02am and a step change of 1.2 MW happens at 12:02am; during the valley load time, the load is set at 1.9 MW from 23:00–23:02, and a step change of 0.8 MW happens at 23:02. Under the three operation scenarios, the simulation results are shown in Figs. 9-11. It can be seen from the three figures that in all the operation conditions, the balance between the demand and the supply can be achieved: during the peak load times, the BESSs are responsive to fill the gap between the generation and the load; meanwhile, the BESSs are also adaptive to shift from the discharging mode to the charging mode when there are generation spikes that make the generation larger than the demand, as shown in the green areas in Fig. 10; during the valley load times when the load level is lower and there is no PV generation, the power generation surplus is consumed by the BESSs, and the BESSs can also change to the discharging mode immediately when there is temporary power shortage due to wind speed variation. Therefore, the proposed scheme can properly and dynamically coordinate the generation units to meet the load demand.

4.2. Case 2: Achieving four control objectives

Next we test the effectiveness of the proposed scheme in achieving the prescribed four optimization objectives. In solving the optimization problem (14)-(23), and (24)-(27), the Tabu search algorithm is utilized by prescribing the charging or discharging solutions of the BESSs in the longer time frame of a day; in this process, the day-ahead market energy price is the same as that in Fig. 7. To achieve the coordination of the
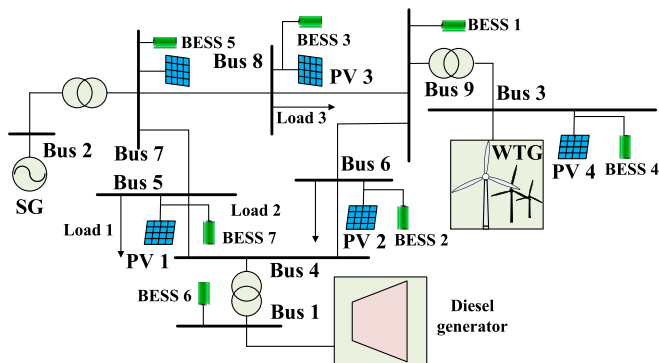
Fig. 8. Modified IEEE 9-Bus system.
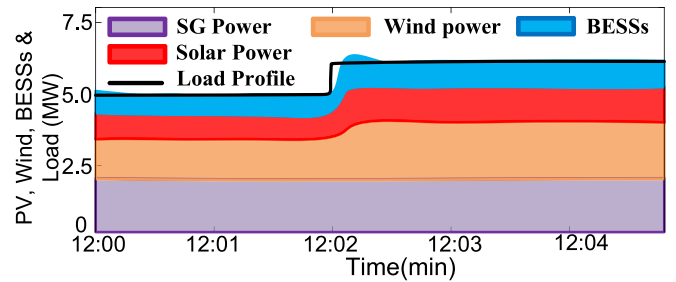
Fig. 9. Coordination result under peak load time and steady wind speed.
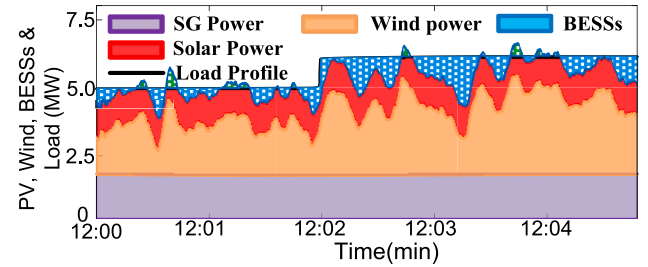

Fig. 10. Coordination result under peak load time and variable wind speed.
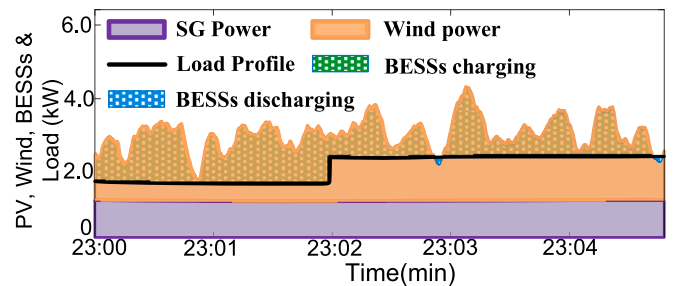

Fig. 11. Coordination result under valley load time and steady wind speed.

control objectives and avoid the conflicts between them, it is necessary to specify their priority degree. As a matter of fact, the missions of voltage and frequency regulation should be treated as short time frame objective as they both deal with the instantaneous term of the system, while the objectives of load shaving and economic benefits should be treated in a longer time frame as they deal with the daily operation of the grid. Therefore, the missions of voltage and frequency regulation should be given higher priority than the other two objectives. Moreover, the mission of voltage regulation should be fulfilled by the BESS at the local level, while the frequency regulation mission should be accomplished by all the BESSs at the global level. Thus, these two missions are parallel to each other without any conflicts. For the remaining two objectives, we give economic benefits higher priority than that of peak shaving. With respect to the operation conditions, it is assumed that the PVs are operating in a sunny summer day and the wind speed is variable; meanwhile, the system load is assumed to be a typical residential load when the peak demand happens at 12:00 and 20:00; in the meantime, it is assumed that a load step change happens at 15:00. The total load curve is shown in Fig. 12.

With such settings, the simulation and numerical results for achieving the four control objectives are given in Figs. 13-16. Among them, Fig. 13 shows the voltage curves of the bus which is connected with PV station. Evidently, when the BESS is located at the PV bus, the bus voltage can be regulated within the threshold, even if the PV generation reaches its maximum level during the noon period. Fig. 14 shows the frequency curve of the grid with different schemes, which fully
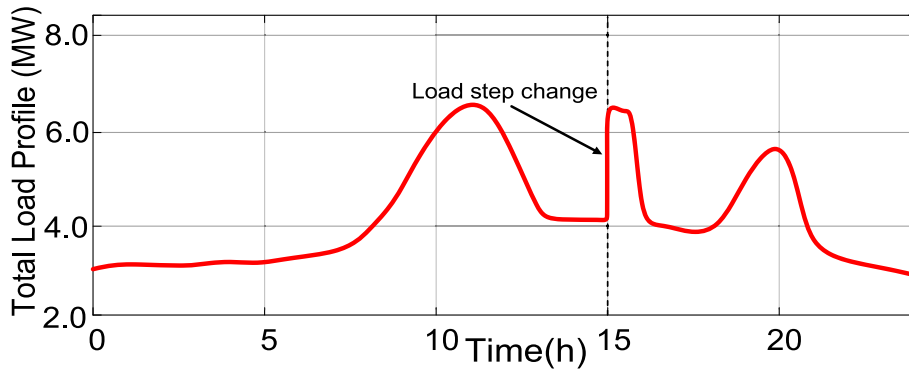
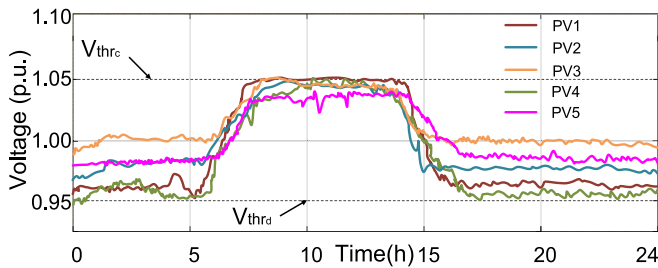**Fig. 12.** Whole day load profiles utilized in simulation.

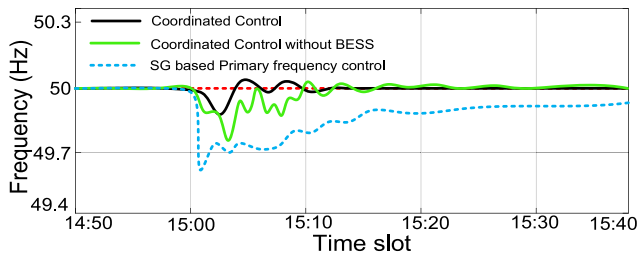**Fig. 13.** Voltage curves of the PV-connected buses.

Fig. 14. Frequency regulation results utilizing different approaches.
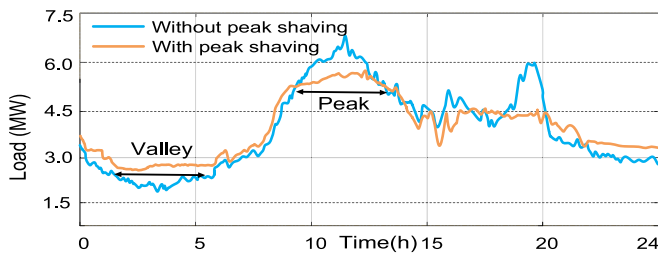

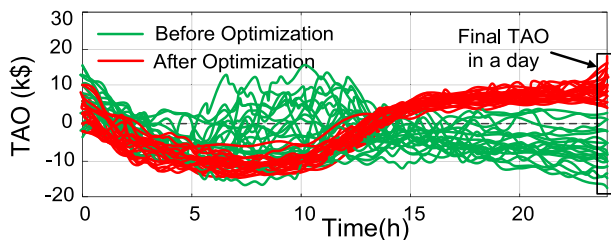**Fig. 15.** Simulation results for peak load shaving and valley filling.

Fig. 16. TAO index of a day before and after optimization in 100 cases.

shows the effectiveness of the BESS based scheme. Fig. 15 presents the load profiles with and without the peak shaving algorithm. Apparently, when the BESSs serve as both energy suppliers and users based on the load level, the peaks of the load can be shaved during noon times and the load valley can be filled during low load period. Fig. 16 shows the curve of the TAO index throughout a whole day in 100 cases with different load profiles, where the TAO value is dynamically changing and the TAO value of the next time slot is the integral results of all the previous time slots. It can be seen that in all the 100 cases, when a day ends, namely, at time slot 24:00, the TAO values after optimization become positive, while those without optimization are negative. Moreover, under all cases with the optimization approach, the curves of TAO change in a coherent manner, which validates the effectiveness and robustness of the proposed scheme.

Fig. 17 shows the SoC of the BESSs at two different time period. Among all the BESSs, BESS 1 and BESS 2 in Fig. 8 are selected as the leaders for frequency and voltage regulation, respectively. Observing Fig. 17, we can easily obtain these findings: during the peak generation period of PV from 11:00 to 12:00, as leader 2—BESS2 is connected with a PV station at Bus 6, it is capable of spontaneously charging to prevent the overvoltage at Bus 6; in the meantime, it is capable of leading the other BESSs connected with PVs, namely, BESS 3, 4, 5 and 7 to shift to the charging mode, while BESS 1 and BESS 6 will stay in the stand-by status as they are not connected with any PV stations. When the load comes to the peak at 12:30, all the BESSs react collectively to fill the demand–supply gap, and the consensus status is achieved in a fast manner. Fig. 17(b) shows the dynamics of the SoC during the valley load times. It can be seen that when the load level is low during midnight, the SoC of the BESSs are contained by the two leading BESSs, which fully
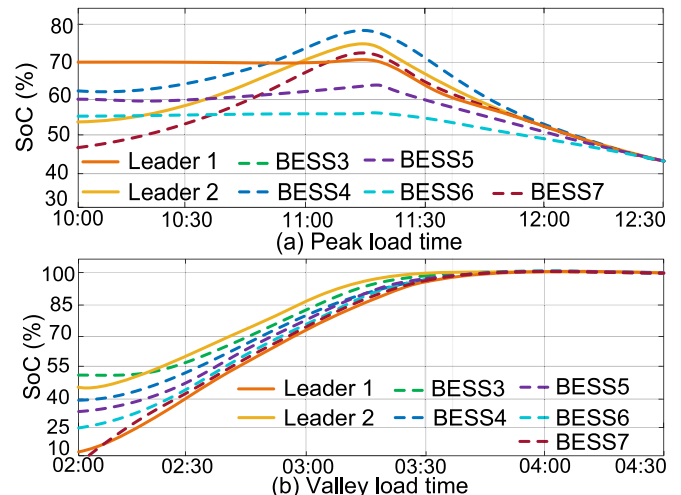

Fig. 17. SoC of BESSs during different time period.

validates the effectiveness of the proposed FTCC.

4.3. Case 3: Performance comparison

To comprehensively evaluate the performance improvement of the proposed scheme on basis of the traditional as well as the state-of-the-art approaches, we conduct a comparative study at this place. In this study, the voltage-droop control + consensus control (VDC + CC) approach from [16], and the fast frequency response + active/reactive power response (FFR + ACR) method from [31] are adopted for comparison purpose. The system operation condition remains the same as that of case 2 and the same daily load curve shown in Fig. 12 is utilized to test the performance. Moreover, we compared the results of the three methods with those when no extra control is applied to the BESSs to regulate the bus voltage and the grid frequency. The results of the four schemes are shown in Figs. 18-19. Among them, Fig. 18 shows the voltage regulation results of the four schemes at bus 6 and bus 8, respectively. It can be seen from Fig. 18 that, as the PV generation reaches its peak at noon, the proposed FTCC can maintain the bus voltage within the upper threshold; the VDC + CC approach also shows similar results in bus voltage regulation, as it mainly utilizes the principle of voltage-droop control; however, the FFR + ACR control and the scheme without extra control shows no capability of controlling the bus voltage, leading to the issue of over-voltage during peak PV generation times.

Fig. 19 shows the frequency regulation results of the four schemes near 15:00 when there is a step load change. It can be seen from Fig. 20 that the proposed FTCC and the FFR + ACR approach are capable of regulating the system frequency in a fast and stable manner, as the time for frequency recovery is short and the frequency curve overshoots are small. Nevertheless, with the other two approaches, the frequency dips are much larger and the system frequency will not recover to the nominal value in short times. Thus, the proposed FTCC approach is capable of simultaneously achieving various different control objectives with equal or better performance comparing with existing methods. Fig. 20 shows the SoC of the BESSs for frequency regulation with the three approaches. Comparing Fig. 20(a) and Fig. 20(b), it can be seen that the VDC + CC approach is not capable of effectively respond to the load change and regulate the system frequency properly; the z, although it can respond to the load change, the BESSs are acting in a disordered manner, which may add to the pressure of BESS status monitoring and regulating.
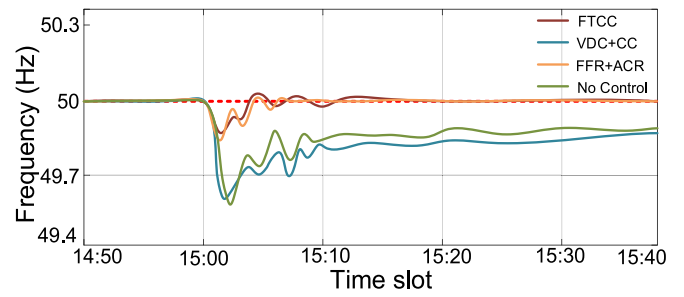

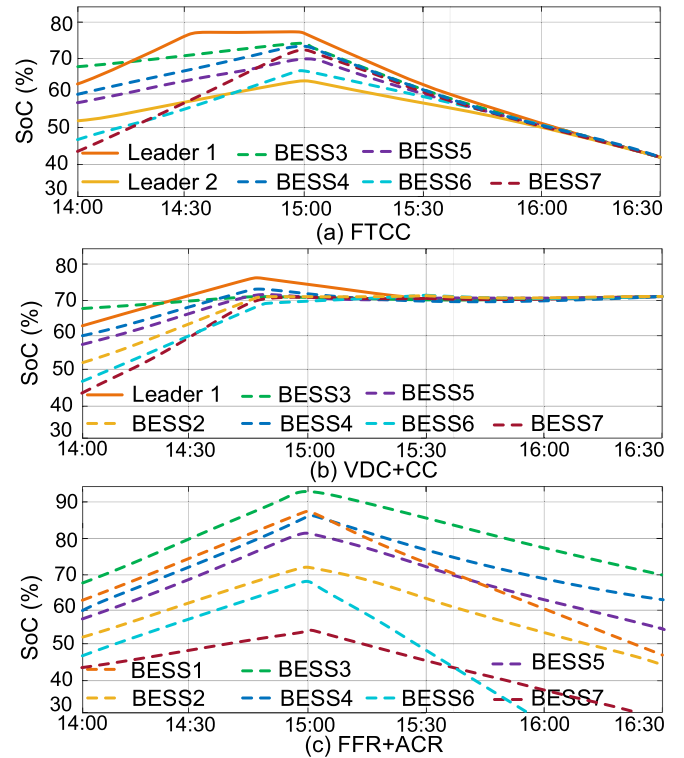**Fig. 19.** Frequency regulation results with four different approaches.

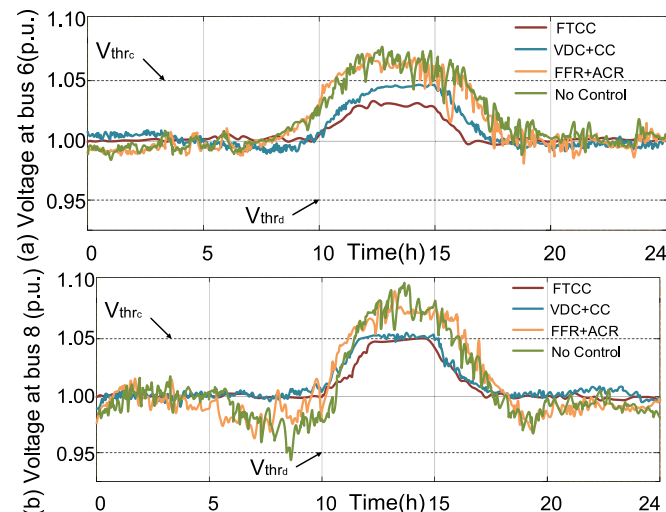**Fig. 20.** SoC of BESSs for frequency regulation with three approaches.

5. Conclusion

This paper proposes a finite time containment control scheme to achieve the coordinated operation of PV, WT and BESSs. Utilizing the advantage of containment control in deciding multiple control dimensions, four control objectives for the weak grid are specified, including bus voltage regulation, grid frequency control, peak load shaving and economic benefits. At first, the optimal sizes of BESSs to fulfill the operation mission requirements are specified; in the meantime, the coordination strategy for the PV, WT and BESS to achieve the timely balance between the demand and supply side is proposed. Subsequently, the predefined four control objectives are modeled and transferred into the operational constraints of the BESSs. Afterwards, the FTCC algorithm is proposed to allow the BESS arrays achieve the containment status within finite time. Simulation case studies are conducted on a modified IEEE 9-bus system to show the effectiveness and performance of the proposed scheme. The simulation results have verified the effectiveness of the proposed scheme in achieving the four control objectives simultaneously, which significantly reduces the complexity and efforts in system configuration especially control system design.

Fig. 18. Voltage regulation results with four different approaches.

CRediT authorship contribution statement

Linyun Xiong: Conceptualization, Methodology, Funding acquisition. **Yinfang Zhu:** Data curation, Formal analysis, Writing-original draft. **Sunhua Huang:** Software, Supervision. **Shiwei Guo:** Investigation, Resources. **Changyu Ban:** Visualization, Formal analysis. **Penghan Li:** Validation. **Muhammad Waseem Khan:** Project administration, Validation. **Tao Niu:** Supervision.

Declaration of competing interest

The authors declare that they have no known competing financial interests or personal relationships that could have appeared to influence the work reported in this paper.

Data availability

Data will be made available on request.

Appendix

Proof of Theorem 1.

First define $\zeta = L_1 e$, where L_1 is given in (35). Then we construct the Lyapunov function $V = \frac{1}{2}\zeta^T Q\zeta$ for stability analysis, where $Q = \text{diag}\{q_1, q_2, \cdots q_n\}$, with $q_i > 0$, such that the matrix $W = QL_1 + L_1^T Q$ is positive-definite and symmetric. Denote $q_{\max} = \max\{q_1, q_2, \cdots q_n\}$, $q_{\min} = \min\{q_1, q_2, \cdots q_n\}$. For the Lyapunov function, its derivative satisfies

$$\dot{V} = -k_1\zeta^T QL_1\zeta - k_2\zeta^T QL_1\tanh\left(\frac{\zeta}{\eta}\right) + \zeta^T QL_2 p_L$$

$$= -\frac{k_1}{2}\zeta^T W\zeta + k_2\sum_{i=1}^{N} q_i\zeta_i^T \sum_{j=1}^{N}(a_{ij}\tanh\left(\frac{\zeta_j}{\eta}\right))q_i\zeta_i^T)$$

$$- k_2\sum_{i=1}^{N} q_i\zeta_i^T \sum_{j=1}^{N+M} a_{ij}\tanh\left(\frac{\zeta_j}{\eta}\right) - \sum_{i=1}^{N} q_i\zeta_i^T \sum_{j=N+1}^{N+M} a_{ij}p_j$$

$$\leqslant -\frac{k_1}{2}\zeta^T W\zeta + k_2 N q_{\max} H_{\max}\upsilon\eta \tag{A1}$$

In the meantime, we need to note that

$$\frac{1}{2}\zeta^T W\zeta \geqslant \frac{1}{2}\gamma_{\min}(W)\|\zeta\|_2^2 \geqslant \frac{\gamma_{\min}(W)}{q_{\max}}V \tag{A2}$$

Thus, for (A1), we further have

$$\dot{V} \leqslant -\frac{k_1\gamma_{\min}}{q_{\max}}V + k_2 N q_{\max} H_{\max}\upsilon\eta \tag{A3}$$

Hence, for the medium variable ζ, it will enter and stay within the invariant set $\mathscr{S}_1 = \left\{\zeta \mid V \leq \frac{k_2 N q_{\max}^2 H_{\max}\upsilon\eta}{k_1\gamma_{\min}}\right\}$ within finite time range. Meanwhile, we note that $V \geq \frac{1}{2}q_{\min}\|\zeta\|_2^2$, then we have

$$\|\zeta\|_2 \leqslant -\sqrt{\frac{2k_2 N q_{\max}^2 H_{\max}\upsilon}{k_1 q_{\min}\gamma_{\min}(W)}}\sqrt{\eta} \tag{A4}$$

Moreover, utilizing the fact $\widetilde{e} = L_1^{-1}\zeta$, we have

$$\|e_i - e_{di}\|_2 \leqslant \|\widetilde{e}\|_2 \leqslant \|L_1^{-1}\|_2\sqrt{\frac{2k_2 N q_{\max}^2 H_{\max}\upsilon}{k_1 q_{\min}\gamma_{\min}(W)}}\sqrt{\eta} \tag{A5}$$

which completes the proof of theorem 1.

References

[1] International Energy Agency, "Renewables,"2017. Accessed: Jul. 1, 2018. [Online]. Available: https://www.iea.org/publications/renewables2017.

[2] Huang S, Xiong L, Zhou Y, Liu J, Jia Q, Li P, et al. Distributed Predefined-Time Secondary Frequency and Average Voltage Control for Islanded AC Microgrids. IEEE Trans Power Syst 2023;38(5):4191–205.

[3] Australian Energy Market Operator (AEMO), "Fast frequency response in the NEM" Future power system security program, AEMO Information & Support Hub, Tech. Rep., Australia, 2017.

[4] Yan R, Saha TK, Modi N, Masood NA, Mosadeghy M. The combined effects of high penetration of wind and PV on power system frequency response. Appl Energy 2015;145:320–30.

[5] Du P, Makarov Y. Using disturbance data to monitor primary fre- quency response for power system interconnections. IEEE Trans Power Syst 2014;29(3):1431–2.

[6] Dozein MG, et al. "System strength and weak grids: Fundamentals. Challenges, and Mitigation Strategies," 2018;AUPEC2018:1–7.

[7] Australian Energy Market Commission (AEMC), "investigation into system strength frameworks in the NEM," 2020.

[8] Gu RY, Saha T. Review of system strength and inertia requirements for the national electricity market of Australia. CSEE J Power Energy Syst 2019;5(3):295–305.

[9] R. Tonkoski D. Turcotte T. H. M. EL-Fouly Impact of high PV penetration on voltage profiles in residential neighborhoods IEEE Trans Sustain Energy 3 3 2012 518 527.

[10] Kant K, Jain C, Singh B. A hybrid diesel-wind-PV based energy generation system with brushless generators. IEEE Trans Ind Inform 2017;13(4):1714–22.

[11] Balbino AJ, Nora BS, Lazzarin TB. An improved mechanical sensorless maximum power point tracking method for permanent magnet synchronous generator-based small wind turbines systems. IEEE Trans Ind Electron 2022;69(5):4765–75.

[12] Jafarabadi RB, Sadeh J, Popov M. Maximum power point tracking injection method for islanding detection of grid-connected photovoltaic systems in microgrid. IEEE Trans Power Del 2021;36(1):168–79.

[13] L. Xiong S. Yang S. Huang D. He P. Li M. W. Khan et al. "Optimal Allocation of Energy Storage System in DFIG Wind Farms for Frequency Support Considering Wake Effect" *IEEE Trans. Power Syst*. 37 3 2022 2097 2112.

[14] Datta U, Kalam A, Shi J. Battery energy storage system control for mitigating PV penetration impact on primary frequency control and state of charge recovery. IEEE Trans Sustain Energy 2020;11(2):746–57.

[15] Mercier P, Cherkaoui R, Oudalov A. Optimizing a battery energy storage system for frequency control application in an isolated power system. IEEE Trans Power Syst 2009;24(3):1469–77.

[16] Subroto RK, Lian KL, Chu CC, Liao CJ. A fast frequency control based on model predictive control taking into account of optimal allocation of power from the energy storage system. IEEE Trans Power Del 2021;36(4):2467–78.

[17] Zeraati M, Golshan MEH, Gurrero JM. Distributed control of battery energy storage systems for voltage regulation in distribution networks with high PV penetration. IEEE Trans Smart Grid 2018;9(4):3582–93.

[18] Liu X, Aichhorn A, Liu L, Li H. Coordinated control of dis- tributed energy storage system with tap changer transformers for voltage rise mitigation under high photovoltaic penetration. IEEE Trans Smart Grid 2012;3(2):897–906.

[19] Kabir MN, Mishra Y, Ledwich G, Dong ZY, Wong KP. Coordinated control of grid-connected photovoltaic reactive power and battery energy storage systems to improve the voltage profile of a res- idential distribution feeder. IEEE Trans Ind Informat 2014;10(2):967–77.

[20] Singh Y, Singh B, Mishra S. Multifunctional control for PV integrated battery energy storage system with improved power quality. IEEE Trans Ind Appl 2020;56 (6):6835–45.

[21] Tedeschi E, Santos-Mugica M. Modeling and control of a wave energy farm including energy storage for power quality enhancement: the Bimep case study. IEEE Trans Power Syst 2014;29(3):1489–97.

[22] W. Wang Y. He X. Xiong and H. Chen "Robust survivability-oriented scheduling of separable mobile energy storage and demand response for isolated distribution systems" *IEEE Trans. Power Del 2022; 37(5): 3521-3535*.

[23] Tziovani L, Hadjidemetriou L, Charalampous C, Tziakouri M, Timotheou S, Kyriakides E. Energy management and control of a flywheel storage system for peak shaving applications. IEEE Trans Smart Grid 2021;12(5):4195–207.

[24] Xiong L, Huang S, Zhou Y, Li P, Wang Z, Khan MW, et al. "Voltage and Frequency Regulation With WT-PV-BESS in Remote Weak Grids via Fixed-Time Containment Control,". IEEE Trans. Power Syst. 2023;38(3):2719–35.

[25] Peng X, Yao W, Yan C, Wen J, Cheng S. Two-stage variable proportion coefficient based frequency support of grid-connected DFIG WTs. IEEE Trans Power Syst 2020; 35(2):962–74.

[26] Miao L, Wen J, Xie H, Yue C, Lee YJ. "Coordinated control strategy of wind turbine generator and energy storage equipment for frequency support,". IEEE Trans. Ind. Appl. 2015;51(4):2732–42.

[27] IEEE Standard for Interconnecting Distributed Resources With Electric Power Systems, IEEE Standard 1547-2003, 2003.

[28] Gan L, Low SH. "Convex relaxations and linear approximation for optimal power flow in multiphase radial networks,". in Proc. Power Syst. Comput. Conf. 2014:1–9.

[29] Xiong L, Yang S, He Y, Li P, Huang S, et al. Specified time consensus control of ESSs for frequency support with DFIG wind turbines. Int J Electr Power & Energy Syst 2021;135:1–14.

[30] Mei J, Ren W, Ma G. Distributed containment control for la- grangian networks with parametric uncertainties under a directed graph. Automatica 2012;48(4): 653–9.

[31] Dozein MG, Gomis-Bellmunt O, Mancarella P. Simultaneous provision of dynamic active and reactive power response from utility scale battery energy storage systems in weak grids. IEEE Trans Power Syst 2021;36(6):5548–57.